Emergent behaviors of buckling-driven elasto-active structures

Yuchen Xi[a], Tom Marzin[a], Richard B. Huang[a], Trevor J. Jones[a,b], and P.-T. Brun[a]

This manuscript was compiled on November 8, 2024

Active systems of self-propelled agents, e.g., birds, fish, and bacteria, can organize their collective motion into myriad autonomous behaviors. Ubiquitous in nature and across length scales, such phenomena are also amenable to artificial settings, e.g., where brainless self-propelled robots orchestrate their movements into spatial-temporal patterns via the application of external cues or when confined within flexible boundaries. Like their natural counterparts, these approaches typically require many units to initiate collective motion, so controlling the ensuing dynamics is challenging. Here, we demonstrate a novel yet simple mechanism that leverages nonlinear elasticity to tame near-diffusive motile particles in forming structures capable of directed motion and other emergent behaviors. Our elasto-active system comprises two centimeter-sized self-propelled microbots connected with elastic beams. These microbots exert forces that suffice to buckle the beam and set the structure in motion. We first rationalize the physics of the interaction between the beam and the microbots. Then we use reduced-order models to predict the interactions of our elasto-active structures with boundaries, e.g., walls and constrictions, and demonstrate how they can exhibit remarkable emergent behaviors such as maze navigation. These findings demonstrate that allowing and understanding changes in body morphology can enhance the capabilities of active matter systems and enable the design of robotic materials capable of space exploration, adaptation, and complex interactions with their surrounding environment.

active matter | soft robotics | nonlinear elasticity | morphological computation

The study of active matter, living or inert, focuses on understanding the mechanical and statistical properties of systems comprising elements capable of converting energy into movement. The field is particularly interested in identifying the principles governing the emergence of self-organized spatio-temporal patterns on scales larger than individual motile units. Examples range from liquid-crystalline order in bacterial flocks to polar order in a school of fish(1). While common in nature, active matter systems are also amenable to artificial laboratory settings(2–4). Exploring model experimental systems allows a careful investigation of the inner workings of active matter, particularly identifying the onset of collective behaviors and rationalizing pattern formation within bulk ensembles of active particles. Historically, the field has focused heavily on fluids and fluid-like systems(1), making active elastic systems comparatively less explored(5).

In recent years, self-propelled microbots, e.g., Hexbug Nano®(6), have been identified as a tunable and reliable means for developing active structures, e.g., oscillatory tails(7, 8) and active elastic solids(9). The motion of individual microbots is understood as vibrating masses whose frictional contacts cause propulsion(10–12), which can be modeled as self-propelled particles that follow Langevin dynamics on timescales much longer than the vibration frequency of their body. This approach allows for the modeling of microbots dynamics in confined geometries(13, 14) or in a harmonic trap(15). Their collective behaviors and ensuing robotic structures have received particular attention(13, 16–18). In bounded and crowded environments these microbots can display a gas-like behavior(19, 20) or cluster around the edges of boundaries(13, 16, 17). In addition, external cues such as light and magnets(21, 22) can be used to control such robotic swarms, e.g., to form clusters or direct movements. Finally, these robotic structures' physical morphology also plays an important role in their functionality and collective behaviors(11). This concept, formalized as morphological computation, relies on the changes in a soft robot morphology to achieve predetermined and adaptive behaviors without relying on the control algorithms typically found in conventional hard robots (23). While deformability is, by definition, inherent to soft robots, our understanding of those systems remains sparse, particularly in the context of active materials. Overall, effectively and efficiently controlling microbot systems remains an ongoing effort

Significance Statement

Active matter is typically composed of many agents, each consuming energy to propel themselves and, at times, display mesmerizing synchronized motion. These spatial-temporal patterns occur in flocks of starlings and bacteria, schools of fish, self-propelled colloids, swarming robots, etc. In these now classic cases, each agent requires several neighbors for self-organized collective behaviors to emerge. Here, we introduce a system where complex emergent behaviors appear with only a pair of agents whose dynamics are tuned thanks to the knowledge we develop, e.g., allowing them to solve a maze. Functionality is mediated by the deformation of our soft robotic contraptions when interacting with their surroundings, an example of morphological computation that leverages elasticity to augment the capabilities of brainless agents.

Author affiliations: [a]Department of Chemical and Biological Engineering, Princeton University, Princeton, New Jersey 08540, USA; [b]Department of Mechanical Engineering, Carnegie Mellon University Pittsburgh, PA 15124, USA

PTB and TJJ designed the research, all authors performed the research and analyzed the data, YX, TM, TJJ and PTB wrote the manuscrtipt.

Please declare any competing interests here.

[2]To whom correspondence should be addressed. E-mail: pbrun@princeton.edu

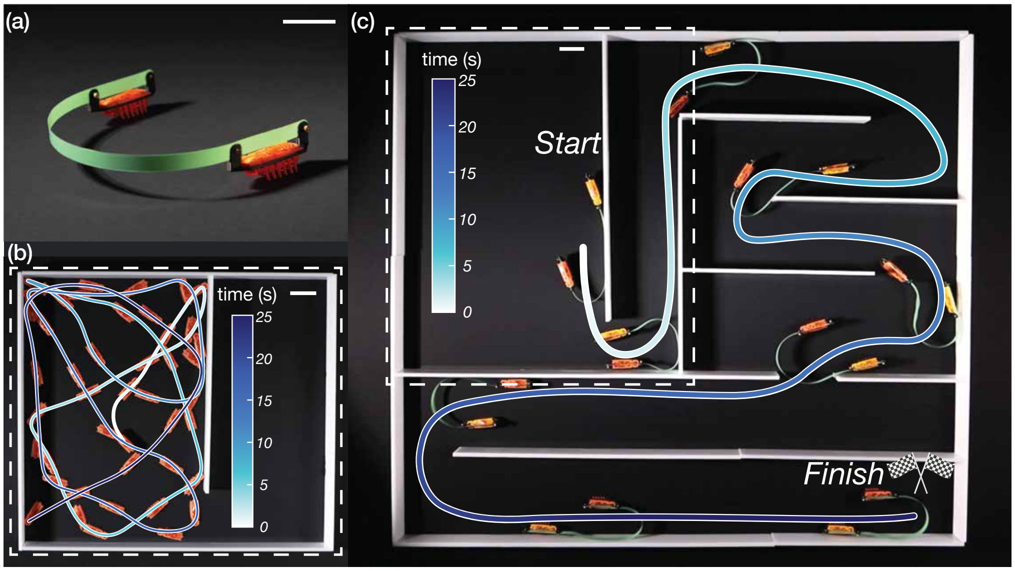

Fig. 1. From mindless particles to emergent behaviors (a) Photograph of the bucklebot, showing two microbots connected by a thin polyester beam. (b) Individual microbot trajectory in a confined space. (c) A bucklebot efficiently navigates a maze within 25 seconds. The dashed area in (c) matches the space shown in (b). (all scale bars are 50 mm in length, and trajectories are color-coded by time).

essential to designing robotic matter capable of achieving predictive and tunable motions. Here, we introduce a new form of autonomous physical behavior by coupling active particles with nonlinear elasticity. Fig. 1(a) illustrates our approach involving two self-propelled microbots connected by an elastic polyester beam. We operate in a regime where the active force exerted by the microbots is sufficient to buckle the connecting beam, thereby aligning the microbots and allowing this contraption, called *bucklebot*, to move across a flat substrate. While individual microbots remain trapped in a confined space for prolonged periods (Fig. 1(b)), a bucklebot manages to solve a maze efficiently, as evident in Fig. 1(c) and Movie S1. Combining experiments and theory, we elucidate the physics governing the dynamics of these bucklebots. We then explore the interaction of bucklebots with physical boundaries, e.g., plane walls and narrow constrictions. Finally, we leverage these quantitative results to elucidate how bucklebots can develop emergent intelligent behaviors such as solving a maze, probing a path, or organizing dispersed particles.

Results

Figure 2 summarizes the main results pertaining to bucklebots evolving in free space. In Fig. 2(a), we show the onset of their motion. Namely, when released, the microbots progressively bend the beam that connects them before assuming a final steady-state configuration characterized by a bending angle ψ and a steady-state velocity V, reached after nearly a second. In Fig. 2(b)-(c), we show the variation of these observables when the length and thickness of the beam are varied. For relatively short and thick (thus stiff) beams, the angle ψ remains close to zero, and the structure barely moves. For longer and thinner (thus soft) beams, the force exerted by the microbots is sufficient to buckle the beam, increasing ψ until the limit value of $\pi/2$ is approached. At this point, the microbots are parallel, facing the same direction and moving at a speed close to their free velocity V_f. The value of V_f is typically related to the force exerted by the microbots and the friction between the structure and the substrate, $V_f = F/\gamma$ where F is the microbot force and γ is the effective drag coefficient acting on the microbots(24).

We recast our experimental data in dimensionless form using V_f as our speed gauge and B/ℓ^2 as the force gauge that captures the beam resistance to bending, where B is the bending stiffness and ℓ is the length of the beam. In Fig. 2(b)-(c), we show that our data collapse to a single master curve, confirming the relevance of the rescaled force $F\ell^2/B$ in predicting the system behavior. Our experiments show a non-zero velocity and bending angle even for small values of $F\ell^2/B$. While the microbots cannot buckle the beam, the bucklebot slides or rotates slowly due to the vibrations from the motor. As $F\ell^2/B$ increases, both ψ and V increase until they reach a plateau around $F\ell^2/B \simeq 50$. Our model, which combines the Kirchhoff equations for elastic beams with a force and moment balance for microbots (see SI Eqn. 1-2), favorably recovers this transition and the overall variation in geometry and speed. The difference between experiment and theory is attributed to a finite size effect: the microbots are not point masses, so a third dimensionless number $\lambda = L/\ell$ is introduced to describe their length relative to that of the beam. In the limit case where $\lambda \simeq 0$, the transition between static and translation occurs at $F\ell^2/B \simeq 10$, in agreement with Euler's critical load for column ends with hinge-hinge boundary conditions(25).

In contrast, for larger values of λ, the microbots exert higher lever-arm torques onto the beam, diminishing the critical buckling load (See SI Section E). This effect is evident in the inset of Fig. 2(b)-(c), where theory curves and experimental data alike are staggered according to the value of λ. The fair agreement between data and model shows the validity of our simplified model. Reality is far more complex, as the twelve microbot legs repeatedly interact and exchange

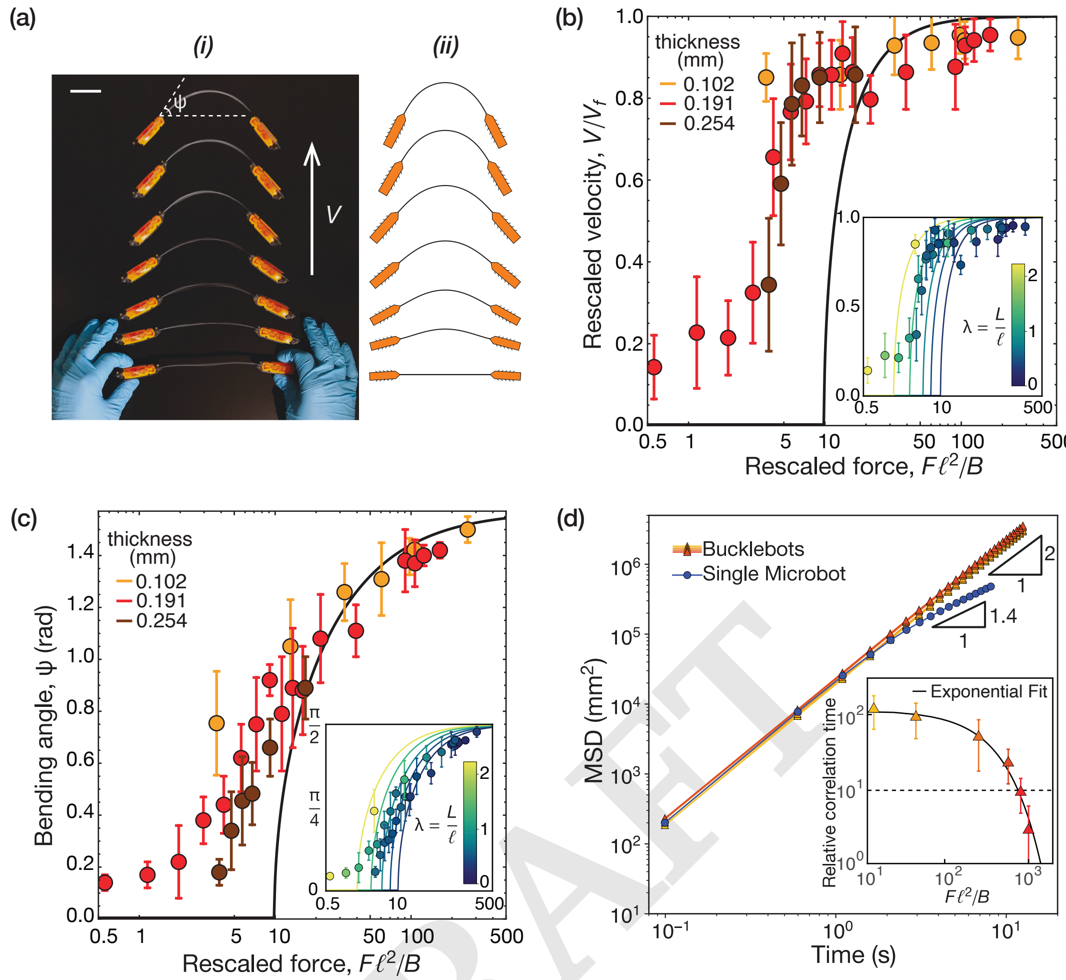

Fig. 2. Dynamics and characterization of bucklebots: (a) (i): Timelapse of a bucklebot with $\Delta t = 0.1s$ (scale bar=50 mm); (ii) Bucklebot dynamics obtained by integrating our model (SI Section A-C). (b) Rescaled velocity V/V_f and (c) bending angle ψ versus rescaled force $F\ell^2/B$. The markers are color-coded by beam thicknesses. The black line represents the predicted steady-state solution with $\lambda \simeq 0$ (SI Section D). Insets: same sets of experiment data color-coded by λ. Lines represent the steady-state solutions when taking into account the finite-size effect ($\lambda > 0$). (d) Log-log plot of the mean squared displacement (MSD) versus time for a single microbot (blue), bucklebots with $F\ell^2/B \simeq$ 10, 40, 240, 600 (oranges from light to dark, respectively). Inset: estimated relative correlation time versus $F\ell^2/B$. The solid black line is an exponential fit from the data points, and the dashed black line is the correlation threshold (10τ, with τ the single microbot reorientation time).

momentum with the substrate. The resulting center of friction does not always align with the microbot center of mass. Nevertheless, the so-called self-aligning torque(9, 15, 26) that results from the discrepancy between those two points appears to have a negligible effect on our system.

Having understood the shape and equilibrium velocity of our bucklebots we move to describe their long-term behavior. In Fig.2(d) we calculate their mean square displacement MSD $= \langle|\boldsymbol{r}(t) - \boldsymbol{r}(0)|^2\rangle$, where $\boldsymbol{r}(t)$ is the position vector at time t, and $\langle\cdot\rangle$ denotes the average value over of all recorded trajectories. In Fig. 2(d), we plot the MSD of bucklebots with rescaled forces ranging from 10 to 600 together with that of single microbots. Single microbots show diffusive-like behavior resembling a noisy walker(27) with a reorientation time $\tau \simeq 1.3$ s and long-term MSD $\propto t^{1.4}$. In contrast, the bucklebots translate ballistically (MSD $\propto t^2$) in the range of the time ($>10\tau$) we probed. Bucklebots achieve persistent directed motion despite the direction changes typically observed in each unit. This result remains true for $10 < F\ell^2/B < 600$. However, past this upper limit, the diffusive nature and inevitable differences between the two microbots become noticeable in experiments. In such high-force regimes, the beam's internal resistance to bending is negligible and thus insufficient to align with the motions of the microbots. As evident from Fig. S4, bucklebots with $F\ell^2/B \simeq 800$ form noticeably curved trajectories. At even higher force regimes ($F\ell^2/B \simeq 1000$), the microbots tend to buckle the beam to its second (and higher) buckling modes, so the bucklebot rotates while slowly translating, demonstrating slower movement and covering two orders of magnitude smaller areas throughout the measurement (see Fig. S4 and Movie S2). In the inset of Fig. 2(d), we report the relative correlation time for bucklebots, defined as the average time when the velocity vector first appears opposite to its initial direction, rescaled by the reorientation time of the single microbot. The inset shows the decay of such time as $F\ell^2/B$ increases. Initially above 100 times the reorientation time of single microbots, this timescale drops

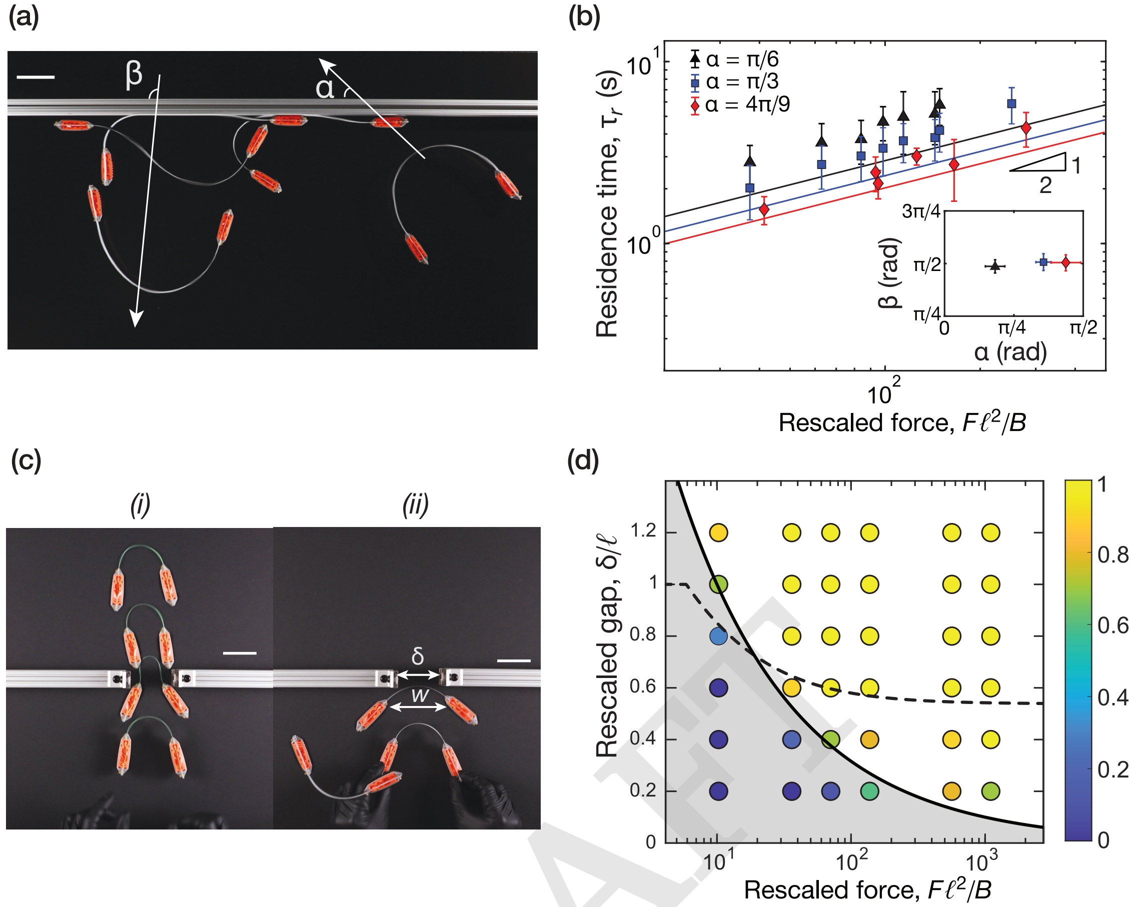

Fig. 3. Bucklebots interacting with boundaries (a) Overalyed photographs of bucklebot with $F\ell^2/B \simeq 60$ approaching a flat wall with angle α, following the wall for some time τ_r, and bouncing off with a reflection angle β (scale bar=50 mm). (b) Residence time, τ_r versus $F\ell^2/B$ for three sets of α. Markers represent experiments (triangles: $\alpha = \pi/6$, squares: $\alpha = \pi/3$, diamonds: $\alpha = 4\pi/9$). Lines are the predictions from the self-oscillation model (see SI Section G). The error bars represent the standard deviation of τ_r for each bucklebot. The inset shows β versus α. (c) Snapshots of passage through a slit of width $\delta = 6$ cm. (i): a bucklebot with $F\ell^2/B \simeq 140$ and (ii) with $F\ell^2/B \simeq 13$ (scale bar=50 mm). (d) Success of passage through the slits over ten launches, shown as a function of rescaled gap size δ/ℓ and $F\ell^2/B$. The experiment data is color-coded by the success rate of passage, as shown by the right color bar. The dashed line indicates the equilibrium width of the free bucklebot (see SI Section D), and the solid line corresponds to our model (SI Eqn. 27). The shaded gray area is our prediction for the region where the bucklebots are expected to bounce off from the slit.

below 10τ beyond $F\ell^2/B \simeq 800$, and eventually reaches values close τ for $F\ell^2/B \simeq 1000$, confirming the negligible influence of the beam in this range. In the following, we focus on bucklebots with $F\ell^2/B$ ranging from 10 to 800 and probe their interactions with boundaries.

We first turn our attention to the interaction of a bucklebot with a plane boundary (see Fig. 3(a)). The bucklebot approaches the wall with an angle α and is found to follow the wall for some residence time τ_r before reflecting off with an angle β. In Fig. 3(b), we find that the reflection angles β are consistently around $\pi/2$, irrespective of the value of α. However, the residence time τ_r increases as α decreases. Shallower approaches stay longer along the wall than a direct hit. Additionally, we find that $\tau_r \propto \sqrt{F\ell^2/B}$. To rationalize such a scaling law, we observe that the microbot in contact with the wall is typically slower than the other one, presumably because of the added friction. As such, the faster outer microbot overtakes its slower counterpart and forces the beam to snap (See Movie S3). Inspired by such behavior, we introduce the limit case scenario, where one single microbot is attached to an elastic beam clamped on one end. We model the ensuing oscillatory dynamics (See SI Eqns. 28-29) and recover the scaling law observed in experiments, as indicated by the solid lines in Fig. 3(b). Our model underpredicts our data since, in our experiment, the bucklebot at the wall is not clamped but instead slides, thereby delaying the beam's oscillation.

Next, we turn to study the passage of a bucklebot through constrictions. Figure 3(c)(i) illustrates the bucklebot ability to deform and pass a tight slit with opening $\delta < w$, with w the bucklebot width. If the beam is too stiff or the slit is too small, the buckle-bot will bounce off the constriction (See Figure 3(c)(ii)). Those results are formalized in Figure 3(d), where we report the probability of successful passage as a function of the gap size rescaled by the beam length, δ/ℓ, and the rescaled force, $F\ell^2/B$. As evident from the figure, larger slits, and larger forces correlate with a higher probability of successful passage. In red, we show the bucklebot equilibrium width w/ℓ. The region below (resp. above) w/ℓ indicates slits smaller (resp. larger) than the equilibrium width. All the trials above this curve have a 100% chance of passing (we send our robots straight onto the slit). However, a sizable region below the

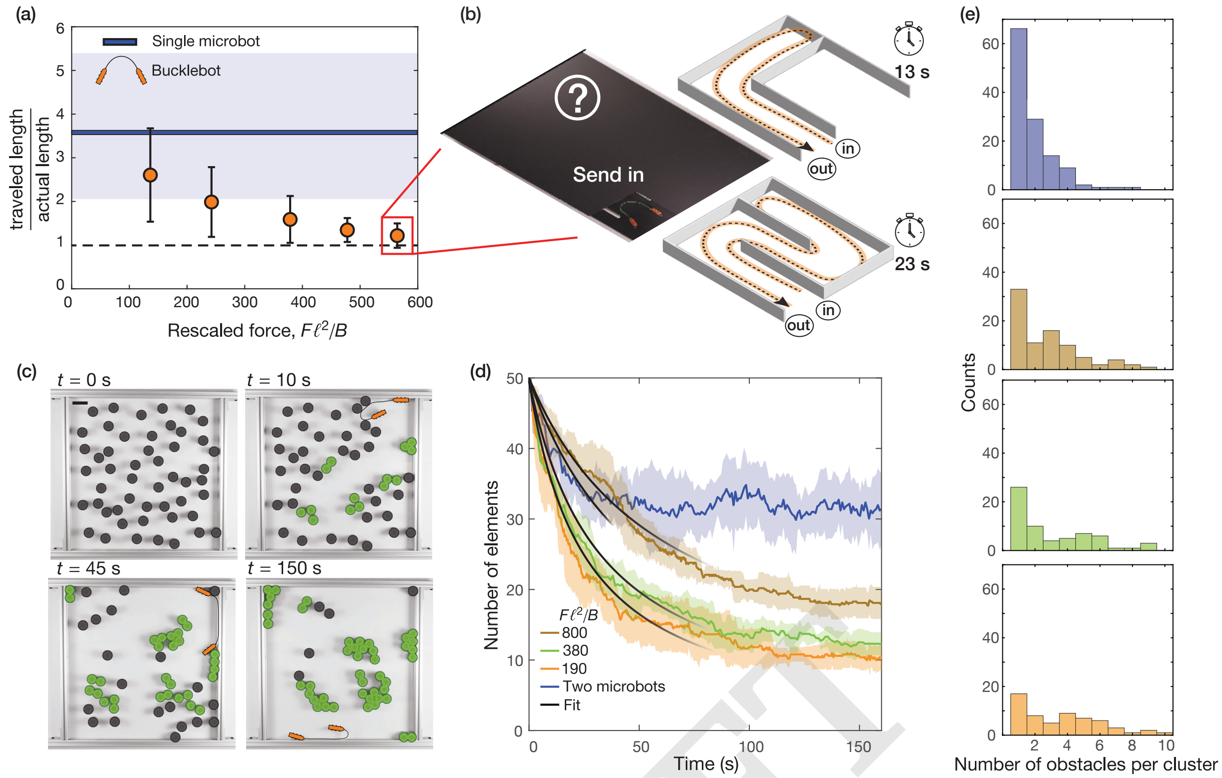

Fig. 4. Leveraging bucklebot emergent behaviors: (a) Traveled length over actual path length is plotted for bucklebots with a wide range of $F\ell^2/B$. Error bars show the standard deviation of bucklebots' traveled lengths. The solid blue line shows the benchmark for a single microbot and the shaded blue area is its error range. (b) The left snapshot shows a probing experiment: a bucklebot with $F\ell^2/B \simeq 560$ is sent into a covered closed path. The schematic drawings show two paths (longer/shorter) the bucklebots can probe and differentiate. In 14 and 25 seconds, the bucklebot reappears at the starting point of the shorter and longer path, respectively. (c) Snapshots of the evolution of a confined room stored by a bucklebot with $F\ell^2/B \simeq 380$. The black circles denote isolated obstacles and the green boundaries correspond to formed clusters. (d) The number of elements representing single or connected obstacles is plotted against time in separate cases of two single microbots and three bucklebots with $F\ell^2/B \simeq$ 800 (brown), 380 (green), and 190 (orange). Each shaded area denotes the standard deviation within 5 trials. Black lines fit the initial decay with a theory derived from the coagulation theory. (e) Size distribution of the formed cluster within the four cases.

curve also sees significant success. We rationalize this region boundary of such success by considering the minimal length the microbots can bend the structure, i.e., $\pi\sqrt{B/F}$, which coincides with the width of the smallest slits that bucklebots can pass.

Discussion

To summarize, our bucklebots, consisting of two self-propelled microbots coupled by a soft elastic beam, achieve persistent ballistic motions, follow walls, and squeeze their deformable structures through narrow constrictions. The combination of these unique capabilities allows them to perform tasks that individual microbots cannot achieve, such as solving a maze (Fig. 1(c)). In the remaining, we leverage these emergent abilities and demonstrate that the bucklebots can accomplish a broad range of tasks.

When sent into a closed path, a bucklebot will navigate to the closed end, bounce back, and reappear at the starting point (see Movie S4). In Fig. 4(a), we show that the ratio between the length traveled by the robots rescaled by the length of the path. While individual microbots travel on average nearly 4 times more than necessary (with nearly 100% variability between trials), we find that our bucklebots converge to the optimal path as $F\ell^2/B$ increases (while dramatically reducing variability). In this limit, our bucklebots can be used to probe and classify simple structures (see Fig. 4(b), where the identification is achieved by recording the entry and exit times).

Likewise, bucklebots differ from the behavior of individual microbots when interacting with obstacles they can displace. In Fig. 4(c), we report a few snapshots of a bucklebot confined with initially dispersed cylindrical obstacles ($N_0 = 50$). The bucklebot ($F\ell^2/B \simeq 380$) pushes these light obstacles and assembles them into clusters. The number of elements saturates in about a minute. In Fig. 4(d), we report the cluster formation dynamics for this bucklebot, together with bucklebots with higher/lower rescaled forces, and contrast it with the situation where two microbots freely travel into a similar enclosure. In all cases, we observe an initial decrease in dispersed elements, N, before reaching saturation. All bucklebots store over 60% of obstacles into clusters, with the lower force bucklebot storing nearly 80%, while two microbots only store 38% of them. Decreasing the rescaled force decreases the final number of clusters and allows a faster initial decay, suggesting that low-force bucklebots can perform such tasks more efficiently. However, bucklebots with even lower rescaled forces ($F\ell^2/B < 190$) tend to get stuck at the enclosure's edges due to their rigidity. Further differences arise when fitting the initial decay with a Smoluchowski-like equation for coagulation(28), $N(t) = N_0/(1 + t/\tau_c)$. The corresponding coagulation timescale τ_c indicates a faster decay for the relatively low-force bucklebots ($\tau_c = 28.5$ and $23.3s$ for $F\ell^2/B \simeq 380$ and 190, respectively) than for single agents ($\tau_c = 49s$). Fig. 4(e) shows the difference in size distribution of the formed clusters. Single microbots form small clusters with only one or two obstacles. In contrast, bucklebots interact more gently with the clusters, preventing damage and thus facilitating the formation of larger clusters.

We have shown that stochastic self-propelled active particles coupled with nonlinear elasticity can be tamed, forced into ballistic motion, and display various emergent abilities as they interact with different boundaries. These autonomous elasto-active structures carry out all these tasks without directed control. Instead, they do so through modulations of their morphology, which our elastic model captures. This newly gained understanding can be leveraged to achieve and control various tasks, such as maze navigation, probing the length of a path, and collecting cylinders, thereby demonstrating how morphological computing can help enhance the capabilities of simple robotic systems. To conclude, we note that we have developed our approach in idealized laboratory settings. Further work is needed to generalize these ideas to real-world environments, e.g., in rough terrain, and integrate such morphological computation into strategies that use higher-order external controls. From a formal standpoint, we have focused on beam-dominated regimes. Exploring softer systems where activity plays a more prominent role would be an exciting continuation of the present work where subtle effects, e.g., the self-aligning torque(26), would need to be accounted for.

Materials and Methods

Bucklebot design and manufacturing. Our active agents are commercially available battery-powered vibrating microbots (Hexbug Nano). Each microbot has a length of 45 mm, a width of 15 mm, a height of 15 mm, and a mass of 7.5 g. Its motion is generated from an internal vibration of a rotating motor transmitted to 12 soft rubber legs to achieve a speed of approximately 154 ± 15 mm/s. The beams are cut from shim stocks using a laser cutter (Epilog Helix-60 Laser engraver). The shim stocks are made of polyester with an elastic modulus of 2.9 GPa. The thickness and length of such elastic beams are well calibrated to ensure a variation of bending stiffness used in experiments. The collar that is used to connect microbots with elastic beams is designed by Rhino and 3D printed by Prusa i3 printer using poly-lactic acid (PLA) (density $\rho = 1.2$ g/cm^3 and elastic modulus $E = 5$ GPa). The beams are clamped to the collars using Dodge 0-80 .115 inch length inserts and corresponding screws.

Experimental setups and bucklebot tracking. The active force exerted by the microbot is estimated by measuring its pushing force via an Instron 10N load cell. The active force is measured to be 20 ± 3 mN. We choose the microbot pairs with approximately the same free velocity and active force to ensure experiment consistency. It is worth noting that the microbot's manufacturing defects and component variabilities give rise to its biased motion. Experimentally, a biased microbot performs a circular motion, whose radius is given by $R = v_f/\omega_b$, where ω_b is the angular rotation rate. We adopt the criteria from Baconnier et al. (29) and choose the microbots that are not noticeably biased. All experiments are carried out on an acrylic surface. For bucklebots, we change the two microbots' batteries simultaneously to maintain their same relative battery level throughout the experiments. To capture the motion of the microbots and the bucklebots, a Canon EOS 80D camera is held by a frame looking down at a large white cast acrylic sheet from McMaster-Carr on top of the lab table. To track these robots while effectively differentiating each individual from one another, we use binary square fiducial markers, known as ArUco markers, which are synthetic square markers composed of a wide black border and an inner binary matrix that determines its identifier (id). We print out markers with different IDs and attach them to each microbot present in the experiments. With Python's Open Source Computer Vision (OpenCV) package(30), we post-process the recorded videos by tracking the attached markers' position data (x, y, t) with time. For example, our code detects the position (x, y) of the marker's four corners. We calculate the mid-point positions of opposite edges on each marker, which allows us to obtain the orientation vector of the microbots. In addition, the velocity of a single microbot is measured by multiplying its position displacement of consecutive frames with frames per second (fps), which allows us to further calculate the mean velocity by averaging the marker's velocities over time. We estimate a bucklebot's center of mass position as the line's center point that connects the two marker centers.

ACKNOWLEDGMENTS. This work was supported by NSF Grant CMMI 2343539 and NSF Future Manufacturing Grant CMMI 2037097.

1. MC Marchetti, et al., Hydrodynamics of soft active matter. *Rev. modern physics* **85**, 1143 (2013).
2. J Deseigne, S Léonard, O Dauchot, H Chaté, Vibrated polar disks: spontaneous motion, binary collisions, and collective dynamics. *Soft Matter* **8**, 5629–5639 (2012).
3. A Bricard, et al., Emergent vortices in populations of colloidal rollers. *Nat. Commun.* **6**, 7470 (2015).
4. V Narayan, N Menon, S Ramaswamy, Nonequilibrium steady states in a vibrated-rod monolayer: tetratic, nematic, and smectic correlations. *J. Stat. Mech. Theory Exp.* **2006**, P01005 (2006).
5. M Fruchart, C Scheibner, V Vitelli, Odd viscosity and odd elasticity. *Annu. Rev. Condens. Matter Phys.* **14**, 471–510 (2023).
6. Hexbug is a toy automate brand developed and distributed by innovation first, http://www.hexbug.com. (year?).
7. E Zheng, et al., Self-Oscillation and Synchronization Transitions in Elastoactive Structures. *Phys. Rev. Lett.* **130**, 178202 (2023) Publisher: American Physical Society.
8. Y Xia, et al., Biomimetic synchronization in biciliated robots. *Phys. Rev. Lett.* **133**, 048302 (2024).
9. P Baconnier, et al., Selective and collective actuation in active solids. *Nat. Phys.* **18**, 1234–1239 (2022).
10. G Cicconofri, A DeSimone, Motility of a model bristle-bot: A theoretical analysis. *Int. J. Non-Linear Mech.* **76**, 233–239 (2015).
11. MY Ben Zion, J Fersula, N Bredeche, O Dauchot, Morphological computation and decentralized learning in a swarm of sterically interacting robots. *Sci. Robotics* **8**, eabo6140 (2023) Publisher: American Association for the Advancement of Science.
12. D Kim, Z Hao, AR Mohazab, A Ansari, On the Forward and Backward Motion of Milli-Bristle-Bots. *Int. J. Non-Linear Mech.* **127**, 103551 (2020) arXiv:2002.10344 [cs, eess].
13. L Giomi, N Hawley-Weld, L Mahadevan, Swarming, swirling and stasis in sequestered bristle-bots. *Proc. Royal Soc. A: Math. Phys. Eng. Sci.* **469**, 20120637 (2013) Publisher: Royal Society.
14. M Leoni, et al., Surfing and crawling macroscopic active particles under strong confinement: Inertial dynamics. *Phys. Rev. Res.* **2**, 043299 (2020) Publisher: American Physical Society.
15. O Dauchot, V Démery, Dynamics of a self-propelled particle in a harmonic trap. *Phys. review letters* **122**, 068002 (2019).
16. JF Boudet, et al., From collections of independent, mindless robots to flexible, mobile, and directional superstructures. *Sci. Robotics* **6**, eabd0272 (2021) Publisher: American Association for the Advancement of Science.
17. A Deblais, et al., Boundaries Control Collective Dynamics of Inertial Self-Propelled Robots. *Phys. Rev. Lett.* **120**, 188002 (2018) Publisher: American Physical Society.
18. C Scholz, M Engel, T Pöschel, Rotating robots move collectively and self-organize. *Nat. Commun.* **9**, 931 (2018) Number: 1 Publisher: Nature Publishing Group.
19. JF Boudet, et al., Effective temperature and dissipation of a gas of active particles probed by the vibrations of a flexible membrane. *Phys. Rev. Res.* **4**, L042006 (2022) Publisher:

American Physical Society.

20. G DiBari, et al., Using Hexbugs™ to model gas pressure and electrical conduction: A pandemic-inspired distance lab. *Am. J. Phys.* **90**, 817–825 (2022).
21. N Sepúlveda, et al., Bioinspired magnetic active matter and the physical limits of magnetotaxis (2021) arXiv:2111.04889 [cond-mat, physics:physics].
22. S Li, et al., Programming active cohesive granular matter with mechanically induced phase changes. *Sci. Adv.* **7**, eabe8494 (2021) Publisher: American Association for the Advancement of Science.
23. H Hauser, T Nanayakkara, F Forni, Leveraging morphological computation for controlling soft robots: Learning from nature to control soft robots. *IEEE Control. Syst. Mag.* **43**, 114–129 (2023).
24. CA Weber, et al., Long-range ordering of vibrated polar disks. *Phys. Rev. Lett.* **110**, 208001 (2013).
25. B Audoly, Y Pomeau, Elasticity and geometry in *Peyresq Lectures on Nonlinear Phenomena.* (World Scientific), pp. 1–35 (2000).
26. P Baconnier, et al., Self-aligning polar active matter (2024).
27. Étienne Fodor, M Cristina Marchetti, The statistical physics of active matter: From self-catalytic colloids to living cells. *Phys. A: Stat. Mech. its Appl.* **504**, 106–120 (2018) Lecture Notes of the 14th International Summer School on Fundamental Problems in Statistical Physics.
28. SK Friedlander, , et al., *Smoke, dust, and haze.* (Oxford university press New York) Vol. 198, (2000).
29. P Baconnier, "Active elastic solids : collective motion, collective actuation & polarization," Theses, Université Paris sciences et lettres (2023). URL https://pastel.hal.science/tel-04081179.
30. G Bradski, The OpenCV Library. *Dr. Dobb's J. Softw. Tools* (2000).